HYBRID ADAPTIVE/NONADAPTIVE BEAMFORMING FOR ULTRASOUND IMAGING

M. Albulayli *D. Rakhmatov*

ECE Department, University of Victoria, Canada
Email: daler@ece.uvic.ca

ABSTRACT

We propose and evaluate a simple yet effective technique of combining nonadaptive and adaptive beamforming methods aimed to achieve high quality of ultrasound images at low computational cost. Our hybrid beamformer automatically switches between nonadaptive and adaptive beamforming of input data vectors, based on the outcome of the comparison of the input coherence factor against a certain threshold. For illustrative purposes, we used the delay-and-sum (DAS) beamformer as an example of a nonadaptive method, while the Generalized Sidelobe Canceller (GSC) and Adaptive Single Snapshot Beamformer (ASSB) served as two examples of an adaptive method. We have applied our technique to simulated ultrasound images of a 12-point phantom and a point-scattering-cyst phantom, demonstrating substantial computational savings without a significant degradation in the image resolution and contrast, in comparison to the standard GSC-based or ASSB-based beamforming methods.

Index Terms— Array signal processing, ultrasonic imaging, image quality

1. INTRODUCTION

Beamforming techniques generally can be classified into two categories: data-independent (nonadaptive) and data-dependent (adaptive) [1]. The weights of the former are fixed and commonly realized by means of standard window functions (e.g., rectangular, Hamming, Kaiser) determining a balance between the mainlobe width and the sidelobe level, which translates into a balance between the image resolution and contrast [2]. On the other hand, the adaptive beamformer weights depend on the statistics of the input data and can achieve a narrow mainlobe width as well as suppress the sidelobe level, thus improving both the image resolution and contrast. However, such improvements in the image quality come at a high computational cost.

The objective of this work is to reduce the computational load due to adaptive beamforming of ultrasound transducer data, while retaining a high quality of resulting images. Our simple yet effective approach is based on switching between a nonadaptive beamformer and an adaptive one based on the scalar value of the *coherence factor* (CF) that quantifies the relationship between coherent and incoherent components of the input data vector. Our evaluation results (Section IV) are based on the simulated 4-MHz ultrasound images of two distinct types: a 12-point phantom acquired by a 98-element phased array, and a point-scatterer-cyst phantom acquired by a 192-element linear array with 66 active elements. These simulations were performed using the FIELD-II tool [3].

In our simulation studies, for each input data vector, we calculate the corresponding CF value and compare it to a certain threshold, denoted by T_{CF}. If the CF value is below T_{CF}, we use a nonadaptive DAS (delay-and-sum) beamformer; otherwise, we use the standard GSC (Generalized Sidelobe Canceller) that implements an adaptive MVDR (minimum-variance distortionless response) beamformer [1]. Additionally, we have also evaluated an alternative combination using the DAS beamformer and the ASSB (Adaptive Single Snapshot Beamformer) [4]. In both cases, our hybrid scheme turns out to be highly effective despite its simplicity, yielding significant computational savings (between 59% and 99%) without significant degradation in the image resolution and contrast (less than 5%).

2. CONVENTIONAL AND PROPOSED BEAMFORMING METHODS

For a conventional M-element beamforming structure shown in Figure 1, at the sampling instance t, the beamformer output $y(t)$ and output power $P(t)$ are given by [1]:

$$y(t) = \mathbf{w}^H(t)\mathbf{x}(t), \quad P(t) = \mathbf{w}^H(t)\mathbf{R}(t)\mathbf{w}(t), \qquad (1)$$

where $\mathbf{w}(t)$ is the weight vector, and $\mathbf{R}(t) = E[\mathbf{x}(t)\mathbf{x}^H(t)]$ is the spatial covariance matrix. We assume that appropriate delay focusing $[\Delta_1(t), \Delta_2(t), ..., \Delta_M(t)]$ is applied at every t, which yields a real-valued phase-compensated input vector $\mathbf{x}(t)$ with the steering vector $\mathbf{d} = \mathbf{1}$ (i.e., a vector of M 1's). The weight vector of the nonadaptive DAS beamformer is simply $\mathbf{w} = \mathbf{1}/M$. On the other hand, the optimal weights of the MVDR beamformer are such that $P(t)$ is minimized,

The authors thank The Natural Sciences and Engineering Research Council of Canada (NSERC) and the Saudi Arabian Cultural Bureau in Canada for finanical support.

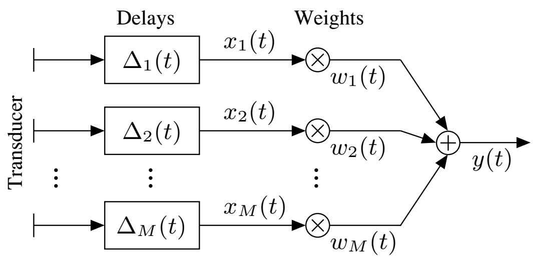

Fig. 1. Conventional ultrasound beamformer.

subject to $\mathbf{w}(t)^H\mathbf{d} = 1$. That is [1]:

$$\mathbf{w}_{\text{opt}}(t) = \frac{\mathbf{R}^{-1}(t)\mathbf{d}}{\mathbf{d}^H\mathbf{R}^{-1}(t)^{-1}\mathbf{d}}. \tag{2}$$

The spatial covariance matrix $\mathbf{R}(t)$ is typically unknown and estimated based on the sample correlation matrix $\widehat{\mathbf{R}}(t) = \frac{1}{N}\sum_{n=t-N+1}^{t}\mathbf{x}(n)\mathbf{x}^H(n)$, where N is the number of snapshots, which is typically very small as ultrasound signals are non-stationary. To decorrelate desired and interfering signals, we also apply the standard spatial smoothing scheme [5]. Letting $\mathbf{x}_k(t) = [x_k(t)\ x_{k+1}(t)\ ...\ x_{k+L-1}(t)]^T$ denote the k-th subarray within $\mathbf{x}(t)$, we have the spatially smoothed sample correlation matrix $\widetilde{\mathbf{R}}(t)$ given by [5]:

$$\widetilde{\mathbf{R}}(t) = \frac{1}{(M-L+1)N}\sum_{n=t-N+1}^{t}\sum_{k=1}^{M-L+1}\mathbf{x}_k(n)\mathbf{x}_k^H(n). \tag{3}$$

Note that the size of $\widetilde{\mathbf{R}}(t)$ is $L \times L$, whereas the original size of $\mathbf{R}(t)$ is $M \times M$. Consequently, replacing $\mathbf{R}(t)$ with $\widetilde{\mathbf{R}}(t)$ in Equation (2) will produce a weight vector $\widetilde{\mathbf{w}}(t)$ of size L (rather than M):

$$\widetilde{\mathbf{w}}(t) = \frac{\widetilde{\mathbf{R}}(t)^{-1}\mathbf{d}}{\mathbf{d}^H\widetilde{\mathbf{R}}(t)^{-1}\mathbf{d}}. \tag{4}$$

The beamformer output is now computed as follows [6]:

$$y(t) = \frac{\widetilde{\mathbf{w}}^H(t)}{M-L+1}\sum_{k=1}^{M-L+1}\mathbf{x}_k(t). \tag{5}$$

One can further enhance the the beamformer output by multiplying it by the coherence factor defined as [7]:

$$\text{CF}(t) = \frac{|\mathbf{d}^H\mathbf{x}(t)|^2}{M\sum_{i=1}^{M}|x_i(t)|^2} = \frac{|\sum_{i=1}^{M}x_i(t)|^2}{M\sum_{i=1}^{M}|x_i(t)|^2}. \tag{6}$$

The CF can be interpreted as the ratio of the on-axis power to the total received power and ranges between 0 and 1. Using the scaled output $\text{CF}(t)y(t)$ has been shown to improve the beamformer performance [7, 8, 9, 10, 11].

Conventional GSC. The MVDR beamformer can be implemented using the GSC structure (see Figure 2), whose output is [1]:

$$y(t) = [\mathbf{w}_q - \mathbf{B}\mathbf{w}_a(t)]^H\mathbf{x}(t), \tag{7}$$

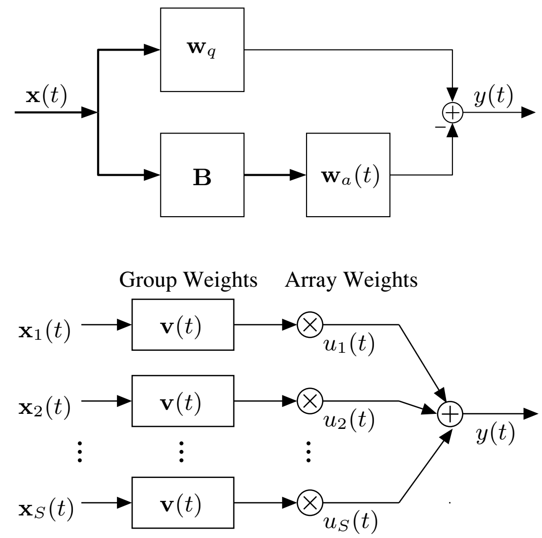

Fig. 2. Conventional GSC (top) and ASSB (bottom).

where $\mathbf{B}$ is the blocking matrix, and $\mathbf{w}_q$ and $\mathbf{w}_a(t)$ are the quiescent and adaptive weight vectors, respectively. Due to delay focusing (i.e., $\mathbf{d}$ is a vector of M 1's), $\mathbf{w}_q$ and $\mathbf{B}$ are fixed, while $\mathbf{w}_a(t)$ varies adaptively. Taking into account spatial smoothing, the optimal weights and the output of the GSC are given by:

$$\widetilde{\mathbf{w}}_a(t) = 2\widetilde{\mathbf{H}}(t)^{-1}\widetilde{\mathbf{B}}^H\widetilde{\mathbf{R}}(t)\widetilde{\mathbf{w}}_q, \tag{8}$$

$$y(t) = \frac{[\widetilde{\mathbf{w}}_q - \widetilde{\mathbf{B}}\widetilde{\mathbf{w}}_a(t)]^H}{M-L+1}\sum_{k=1}^{M-L+1}\mathbf{x}_k(t), \tag{9}$$

where $\widetilde{\mathbf{H}}(t) = 2\widetilde{\mathbf{B}}^H\widetilde{\mathbf{R}}(t)\widetilde{\mathbf{B}}$. Note that $\widetilde{\mathbf{B}}$, $\widetilde{\mathbf{w}}_q$, and $\widetilde{\mathbf{w}}_a(t)$ correspond to the original counterparts $\mathbf{B}$, $\mathbf{w}_q$, and $\mathbf{w}_a(t)$, whose dimensions have been reduced due to spatial smoothing.

Conventional ASSB. The ASSB represents a different approach to the rejection of nonstationary and coherent interferers [4]. One possible ASSB structure (used in this work) is shown in Figure 2, where the input vector $\mathbf{x}(t)$ is divided into overlapping L-element subvectors $\mathbf{x}_k(t)$. As in the case of spatial smoothing, we let the number of such subvectors be $S = M - L + 1$, where $L = M/2$. The ASSB output is [4]:

$$y(t) = \mathbf{u}^H(t)\mathbf{X}(t)\mathbf{v}(t), \tag{10}$$

where each row k in the $S \times L$ data matrix $\mathbf{X}(t)$ is $\mathbf{x}_k^T(t)$. The data matrix $\mathbf{X}(t)$ can be interpreted as the superposition of a desired signal $s_1(t)$ and $(K-1)$ interfering signals $s_2(t), s_3(t), ..., s_K(t)$ impinging on the array, i.e., $\mathbf{X} = \sum_{i=1}^{K}\mathbf{a}_i\mathbf{g}_i^T s_i(t)$, where $K \leq L$ [4]. For each signal s_i arriving at an angle θ_i, we have the corresponding S-element array characteristic vector $\mathbf{a}_i$ and L-element group characteristic vector $\mathbf{g}_i$. Applying appropriate delay focusing (based on θ_1 of the desired signal s_1) yields $\mathbf{a}_1 = \mathbf{1}$ (i.e., a vector of S 1's) and $\mathbf{g}_1 = \mathbf{1}$ (i.e., a vector of L 1's).

It has been shown in [4] that the beamforming problem in the presence of noise can be formulated as

$$\min_{\mathbf{v},y} \|\mathbf{e}\|_2^2 \,, \text{ subject to } \begin{bmatrix} \mathbf{g}_1^T & 0 \\ \mathbf{X}(t) & -\mathbf{a}_1 \end{bmatrix} \begin{bmatrix} \mathbf{v}(t) \\ y(t) \end{bmatrix} = \begin{bmatrix} 1 \\ \mathbf{e} \end{bmatrix}. \quad (11)$$

Using Lagrange multipliers, we obtain the following solution:

$$\mathbf{c} = \frac{(\mathbf{A}^H\mathbf{A})^{-1}\mathbf{b}}{\mathbf{b}^H(\mathbf{A}^H\mathbf{A})^{-1}\mathbf{b}}, \quad (12)$$

where $\mathbf{A} = \begin{bmatrix}\mathbf{X}(t) & -\mathbf{a}_1\end{bmatrix}$, $\mathbf{b} = \begin{bmatrix}\mathbf{g}_1 \\ 0\end{bmatrix}$, and $\mathbf{c} = \begin{bmatrix}\mathbf{v}(t) \\ y(t)\end{bmatrix}$. Note that the last element of $\mathbf{c}$ is the desired beamformer output.

Adaptive/Nonadaptive Hybrid Method. The nonadaptive DAS beamformer has a low computational cost, but yields images of low quality. On the other hand, the GSC and ASSB yield high image quality, but have a high computational cost (mainly due to matrix inversions). We propose a straightforward low-cost high-quality beamforming scheme that automatically switches between the nonadaptive DAS-based and adaptive GSC-based or ASSB-based methods. Such a switching decision relies on the coherence factor: very low CF values indicate that the most of the received energy is in the sidelobes, and the image quality not likely to be improved significantly by using an adaptive beamformer as opposed to nonadaptive one. This simple idea is summarized below:

1. Given input vector $\mathbf{x}(t)$, compute CF(t).
2. If CF$(t) \geq T_{CF}$, then use the GSC (or the ASSB) to calculate output $y(t)$, else use the DAS beamformer to calculate $y(t)$.
3. Let $y(t) \leftarrow$ CF$(t)y(t)$.

Let C_a and C_n denote, respectively, the computational costs of adaptive and nonadaptive beamforming per input vector, i.e., the cost of the GSC (or the ASSB) and the DAS beamformer in our case. Also, let V denote the total number of input vectors $\mathbf{x}(t)$ processed to form an image, and let V_a denote the number of input vectors satisfying the condition CF$(t) \geq T_{CF}$ and processed adaptively. Then, in comparison to a conventional always-adaptive beamformer, our hybrid scheme achieves the beamforming computational savings per image given by:

$$\text{Savings/Image} = \left(1 - \frac{V_a}{V}\right)\left(1 - \frac{C_a}{C_n}\right) \times 100\%. \quad (13)$$

The amount of such savings varies depending on the three factors: (1) the beamformer's computational complexity quantified by C_a and C_n, (2) the input data, determining V and affecting V_a via the CF(t) value, and (3) the switching threshold, affecting V_a via the T_{CF} value.

3. EVALUATION RESULTS

In this section, we evaluate the performance of the hybrid DAS/GSC and DAS/ASSB beamformers in comparison to their conventional counterparts. Our evaluations are based on the simulated 4-MHz ultrasound images of a 12-point phantom acquired by a phased array ($M = 98$ and $N = 1$), and a point-scatterer-cyst phantom acquired by a linear array ($M = 66$ and $N = 2$). The simulations were performed using the FIELD-II tool [3] with four different threshold settings: $T_{CF} = 0.01, 0.05, 0.10, 0.15$.

Figure 3 shows the simulated images of the 12-point phantom.[1] To assess the image quality at focus, we rely on the FWHM (full width at half maximum) as an indication of the resolution quality and the sidelobe energy E_{SL} (calculated for attenuation level larger than 25 dB) as an indication of the contrast quality. They are given in Table 1, where lower values are indicative of better-quality imaging. For the hybrid DAS/GSC beamformer, one can see that using $T_{CF} = 0.05$ yields the image of comparable quality (FWHM = 0.3512 mm and $E_{SL} = -36.52$ dB) with respect to the conventional GSC (FWHM = 0.3511 mm and $E_{SL} = -37.15$ dB). Note that using $T_{CF} = 0.10$ or 0.15 significantly degrades E_{SL}; on the other hand, using $T_{CF} = 0.01$ practically matches the performance of the conventional GSC. However, the computational savings achieved with $T_{CF} = 0.01$ are approximately 57%, as opposed to the savings of approximately 95% due to $T_{CF} = 0.05$. Thus, based on Table 1, we conclude that $T_{CF} = 0.05$ is an effective threshold for the hybrid DAS/GSC beamformer. Similarly, comparing the conventional ASSB and the hybrid DAS/ASSB beamformer (see Table 1), we conclude that $T_{CF} = 0.15$ is an effective threshold for the latter. It yields the image of comparable quality (FWHM = 0.3550 mm and $E_{SL} = -29.93$ dB) with respect to the conventional ASSB (FWHM = 0.3533 mm and $E_{SL} = -31.38$ dB), while achieving the computational savings of approximately 99%.

Figure 4 shows the simulated images of the point-cyst-scatterer (PSC) phantom.[2] The contrast values for the scattering region are given in Table 1, where one can see that $T_{CF} = 0.05$ and $T_{CF} = 0.15$ remain effective threshold settings for the hybrid DAS/GSC and DAS/ASSB beamformers, respectively. While maintaining a comparable image quality with their respective conventional counterparts, the hybrid DAS/GSC and DAS/ASSB beamformers achieve computational savings of approximately 59% and 73%, respectively.

Concluding Remarks. One can notice that the hybrid DAS/GSC with $T_{CF} = 0.05$ outperforms the conventional ASSB. However, the hybrid DAS/ASSB with $T_{CF} = 0.15$ is better than the hybrid DAS/GSC with $T_{CF} = 0.15$ when imaging the 12-point phantom beyond the 60-mm focusing

[1] The 12-point phantom consists of 12 single point targets placed at the 10-mm intervals starting at 30 mm from the transducer surface. During transmission, the focus is fixed at 60 mm, and during reception, dynamic receive focusing is performed at 10-mm intervals.

[2] The PSC phantom is placed at 60 mm (transmit focus) and consists of a point target, a highly scattering region with the radius of 1.5 mm, and a water-filled cyst region with the radius of 2 mm. The lateral distances are -14 mm, -5 mm, and 10 mm, respectively. During reception, dynamic receive focusing is performed at 10-mm intervals.

Table 1. Quantitative image quality indicators.

Beamforming Method	12-Point FWHM (mm)	12-Point E_{SL} (dB)	PSC Contrast (Scatterer)
DAS	0.6723	-28.32	2.069
Conventional GSC	0.3511	-37.15	3.438
Conventional ASSB	0.3533	-31.38	3.228
DAS/GSC: $T_{CF} = 0.01$	0.3512	-37.15	3.430
DAS/GSC: $T_{CF} = 0.05$	0.3512	-36.52	3.370
DAS/GSC: $T_{CF} = 0.10$	0.3533	-31.21	3.180
DAS/GSC: $T_{CF} = 0.15$	0.3537	-30.99	2.981
DAS/ASSB: $T_{CF} = 0.01$	0.3533	-31.36	3.214
DAS/ASSB: $T_{CF} = 0.05$	0.3533	-31.28	3.132
DAS/ASSB: $T_{CF} = 0.10$	0.3551	-31.42	3.127
DAS/ASSB: $T_{CF} = 0.15$	0.3550	-29.93	3.126

point (see Figure 3). As for the PSC phantom images (see Figure 4, the hybrid DAS/GSC with $T_{CF} = 0.15$ also yields a slightly lower contrast in the scattering region (due to an increased mean signal in the background speckle) in comparison to the hybrid DAS/ASSB with $T_{CF} = 0.15$. Consequently, one possible recommendation is that an ultrasound system employ GSC-based beamforming as a starting point, but switch to the hybrid DAS/ASSB when the higher values of T_{CF} are chosen. If only a single beamformer is to be used, our evaluation results suggest that the hybrid DAS/GSC with $T_{CF} = 0.05$ is a clear winner in terms of an effective tradeoff between the image quality and computational savings.

4. RELATION TO PRIOR WORK

There is an extensive literature on adaptive beamforming applied to ultrasound imaging, e.g., see [12, 6, 13, 14, 15, 16, 17, 18, 7], most popular choices being the minimum-variance and beamspace beamformers. This paper is the first to provide a relatively detailed evaluation of the ASSB [4] on the simulated ultrasound data, aside from a very brief and somewhat cursory treatment in [19]. To the best of our knowledge, this paper is also the first to explore a CF-based switching scheme between nonadaptive and adaptive beamforming as a means to reduce the system's computational load. Several other methods reported in the literature, e.g. see [20, 21, 22], have aimed at reducing the minimum-variance beamforming complexity via various approximations. Our switching scheme complements rather than competes with those methods: any of the latter can be employed whenever the coherence factor value is detected to exceed T_{CF}. As the next step, this work may be extended in several important directions, such as adaptive threshold control, hybrid broadband beamforming, and hybrid beamforming based on compressed sensing [23, 24, 25].

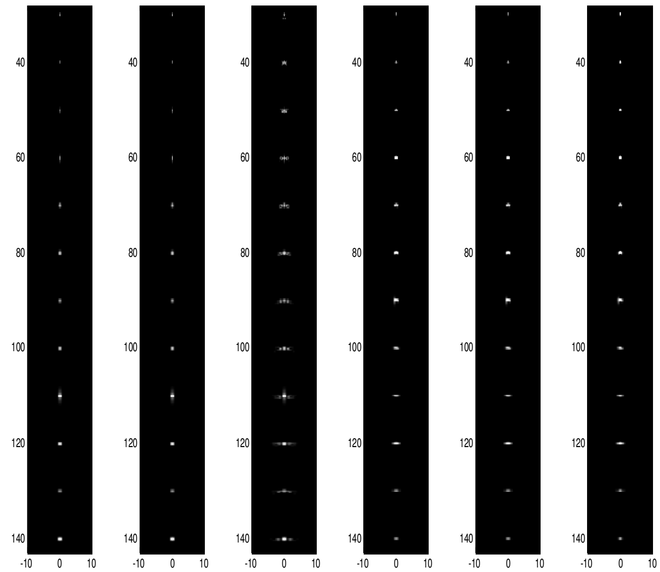

Fig. 3. 12-point phantom. From left to right: GSC, DAS/GSC with $T_{CF} = 0.05$, DAS/GSC with $T_{CF} = 0.15$, ASSB, DAS/ASSB with $T_{CF} = 0.05$, DAS/ASSB with $T_{CF} = 0.15$. Horizontal/vertical axes are lateral/axial distances (mm).

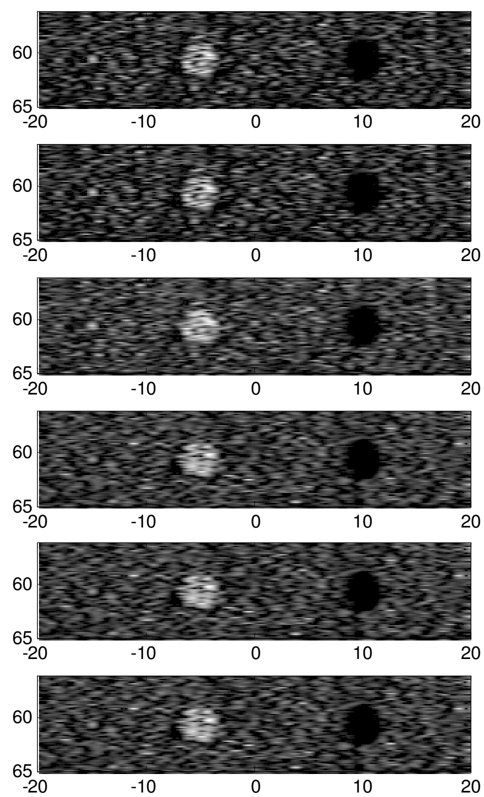

Fig. 4. PSC phantom. From top to bottom: GSC, DAS/GSC with $T_{CF} = 0.05$, DAS/GSC with $T_{CF} = 0.15$, ASSB, DAS/ASSB with $T_{CF} = 0.05$, DAS/ASSB with $T_{CF} = 0.15$. Horizontal/vertical axes are lateral/axial distances (mm).

5. REFERENCES

[1] H. Van Trees, *Optimum Array Processing*, Wiley, NY, 2002.

[2] R. Cobbold, *Foundations of Biomedical Ultrasound*, Oxford, NY, 2006.

[3] J. Jensen, "Field II Simulation Program," 2008, Available online `http://server.elektro.dtu.dk/personal/jaj/field`.

[4] M. Ali and P. Schreib, "Adaptive single-snapshot beamforming: a new concept for rejection of nonstationary and coherent interferers," *IEEE Trans. Signal Processing*, vol. 40, no. 12, pp. 3055–3058, Dec. 1992.

[5] T. Shah and T. Kailath, "Adaptive beamforming for coherent signals and interference," *IEEE Trans. Acoustics, Speech, and Signal Processing*, vol. 33, no. 3, pp. 527–536, June 1985.

[6] M. Sasso and C. Cohen-Bacrie, "Medical ultrasound imaging using the fully adaptive beamformer," in *Proc. IEEE International Conf. Acoustics, Speech, and Signal Processing*, Mar. 2005, pp. 489–492.

[7] C. Nilsen and S. Holm, "Wiener beamforming and the coherence factor in ultrasound imaging," *IEEE Trans. Ultrasonics, Ferroelectrics, and Frequency Control*, vol. 57, no. 6, pp. 1329–1346, June 2010.

[8] K. Hollman, K. Rigby, and M. O'Donnell, "Coherence factor of speckle from a multi-row probe," in *Proc. IEEE Ultrasonics Symp.*, 1999, pp. 1257–1260.

[9] S. Park, A. Karpiouk, S. Aglyamov, and S. Emelianov, "Adaptive beamforming for photoacoustic imaging using linear arrays," in *Proc. IEEE Ultrasonics Symp.*, Nov. 2008, pp. 1088–1091.

[10] S. Wang and P. Li, "MVDR-based coherence weighting for high-frame-rate adaptive imaging," *IEEE Trans. Ultrasonics, Ferroelectrics, and Frequency Control*, vol. 56, no. 10, pp. 2097–2110, Oct. 2009.

[11] Y. Wang and P. Li, "SNR-dependent coherence weighting for minimum-variance beamforming," in *Proc. IEEE Ultrasonics Symp.*, 2011, pp. 2452–2455.

[12] J. Mann and W. Walker, "A constrained adaptive beamformer for medical ultrasound: Initial results," in *Proc. IEEE Ultrasonics Symp.*, Oct. 2002, pp. 1807–1810.

[13] Z. Wang, J. Li, and R. Wu, "Time-delay- and time-reversal-based robust Capon beamformers for ultrasound imaging," *IEEE Trans. Medical Imaging*, vol. 24, no. 10, pp. 1308–1322, Oct. 2005.

[14] J. Synnevag, A. Austeng, and S. Holm, "Adaptive beamforming applied to medical ultrasound imaging," *IEEE Trans. Ultrasonics, Ferroelectrics, and Frequency Control*, vol. 54, no. 8, pp. 1606–1613, Aug. 2007.

[15] F. Viola, M. Ellis, and W. Walker, "Time-domain optimized near-field estimator for ultrasound imaging: initial development and results," *IEEE Trans. Medical Imaging*, vol. 27, no. 1, pp. 99–110, Jan. 2008.

[16] F. Vignon and M. Burcher, "Capon beamforming in medical ultrasound imaging with focused beams," *IEEE Trans. Ultrasonics, Ferroelectrics, and Frequency Control*, vol. 55, no. 3, pp. 619–628, Mar. 2008.

[17] I. Holfort, F. Gran, and J. Jensen, "Minimum variance beamforming for ultrasound imaging," *IEEE Trans. Ultrasonics, Ferroelectrics, and Frequency Control*, vol. 56, no. 2, pp. 314–325, Feb. 2009.

[18] C. Nilsen and I. Hafizovic, "Beamspace adaptive beamforming for ultrasound imaging," *IEEE Trans. Ultrasonics, Ferroelectrics, and Frequency Control*, vol. 56, no. 10, pp. 2187–2197, Oct. 2009.

[19] F. Viola and W. Walker, "Adaptive signal processing in medical ultrasound beamforming," in *Proc. IEEE Ultrasonics Symp.*, Oct. 2002, pp. 1807–1810.

[20] S. Khezerloo and D. Rakhmatov, "Gradient-driven beamforming for biomedical ultrasound," in *Proc. IEEE International Engineering in Medicine and Biology Society Conf.*, Sept. 2009, pp. 444–450.

[21] J. Synnevag, A. Austeng, and S. Holm, "Low-complexity data-dependent beamformer," *IEEE Trans. Ultrasonics, Ferroelectrics, and Frequency Control*, vol. 57, no. 2, pp. 281–289, Feb. 2010.

[22] B. Asl and A. Mahloojifar, "Low-complexity adaptive beamformer for ultrasound imaging using structured covariance matrix," *IEEE Trans. Ultrasonics, Ferroelectrics, and Frequency Control*, vol. 59, no. 4, pp. 660–667, Apr. 2012.

[23] J. Haboba, M. Mangia, F. Pareschi, R. Rovatti, and G. Setti, "A pragmatic look at some compressive sensing architectures with saturation and quantization," *IEEE J. Emerging and Selected Topics in Circuits and Systems*, vol. 2, no. 3, pp. 443–459, Sept. 2012.

[24] N. Wagner, Y. Eldar, and Z. Friedman, "Compressed beamforming in ultrasound imaging," *IEEE Trans. Signal Processing*, vol. 60, no. 9, pp. 4643–4657, Sept. 2012.

[25] Y. Eldar and G. Kutyniok, Eds., *Compressed Sensing: Theory and Applications*, Cambridge, NY, 2012.